Experimental Tests of the Chiral Anomaly Magnetoresistance in the Dirac-Weyl Semimetals Na_3Bi and GdPtBi

Sihang Liang,[1] Jingjing Lin,[1] Satya Kushwaha,[2] Jie Xing,[3] Ni Ni,[3] R. J. Cava,[2] and N. P. Ong[1,*]

[1]*Department of Physics, Princeton University, Princeton, New Jersey 08544, USA*
[2]*Department of Chemistry, Princeton University, Princeton, New Jersey 08544, USA*
[3]*Department of Physics and Astronomy and California NanoSystems Institute, University of California, Los Angeles, California 90095, USA*

(Received 27 November 2017; revised manuscript received 7 June 2018; published 3 July 2018)

In the Dirac-Weyl semimetal, the chiral anomaly appears as an "axial" current arising from charge pumping between the lowest (chiral) Landau levels of the Weyl nodes, when an electric field is applied parallel to a magnetic field **B**. Evidence for the chiral anomaly was obtained from the longitudinal magnetoresistance (LMR) in Na_3Bi and GdPtBi. However, current-jetting effects (focusing of the current density **J**) have raised general concerns about LMR experiments. Here, we implement a litmus test that allows the intrinsic LMR in Na_3Bi and GdPtBi to be sharply distinguished from pure current-jetting effects (in pure Bi). Current jetting enhances J along the mid-line (spine) of the sample while decreasing it at the edge. We measure the distortion by comparing the local voltage drop at the spine (expressed as the resistance R_{spine}) with that at the edge (R_{edge}). In Bi, R_{spine} sharply increases with B, but R_{edge} decreases (jetting effects are dominant). However, in Na_3Bi and GdPtBi, both R_{spine} and R_{edge} decrease (jetting effects are subdominant). A numerical simulation allows the jetting distortions to be removed entirely. We find that the intrinsic longitudinal resistivity $\rho_{xx}(B)$ in Na_3Bi decreases by a factor of 10.9 between $B = 0$ and 10 T. A second litmus test is obtained from the parametric plot of the planar angular magnetoresistance. These results considerably strengthen the evidence for the intrinsic nature of the chiral-anomaly-induced LMR. We briefly discuss how the squeeze test may be extended to test $ZrTe_5$.

DOI: 10.1103/PhysRevX.8.031002

Subject Areas: Condensed Matter Physics, Topological Insulators

I. INTRODUCTION

In the past two decades, research on the Dirac states in graphene and topological insulators has uncovered many novel properties arising from their linear Dirac dispersion. In these materials, the Dirac states are confined to the two-dimensional (2D) plane. Interest in three-dimensional (3D) Dirac states may be traced to the even earlier prediction of Nielsen and Ninomiya (1983) [1] that the chiral anomaly may be observable in crystals (the space-time dimension $3 + 1$D needs to be even). The anomaly, which appears as a current in a longitudinal magnetic field **B**, arises from the breaking of a fundamental, classical symmetry of massless fermions—the chiral symmetry. Recent progress in topological quantum matter has led to several systems that feature protected 3D Dirac and Weyl states in the bulk [2,3].

A crucial step in the search for 3D Dirac states was the realization that inclusion of point group symmetry [with time-reversal (TR) symmetry and inversion symmetry] allows Dirac nodes to be protected anywhere along symmetry axes, instead of being pinned to TR-invariant momenta on the Brillouin zone surface [4,5]. Relaxation of this constraint led to the discovery of Na_3Bi [6] and Cd_3As_2, in which the two Dirac nodes are protected by C_3 and C_4 symmetry, respectively. In the absence of **B**, each Dirac node is described by a 4×4 Hamiltonian that can be block diagonalized into two 2×2 Weyl blocks with opposite chiralities ($\chi = \pm 1$). The absence of mixing between the two Weyl fermions expresses the existence of chiral symmetry. In a strong **B**, the Weyl states are quantized into Landau levels. As shown in Fig. 1(a), a distinguishing feature is that the lowest Landau level (LLL) in each Weyl node is chiral, with a velocity **v** strictly $\|\mathbf{B}$ (or $-\mathbf{B}$ as dictated by χ) [3].

As a result, electrons occupying the LLL segregate into two massless groups—left and right movers, with populations N_L and N_R, respectively. Independent conservation

*Corresponding author.
npo@princeton.edu

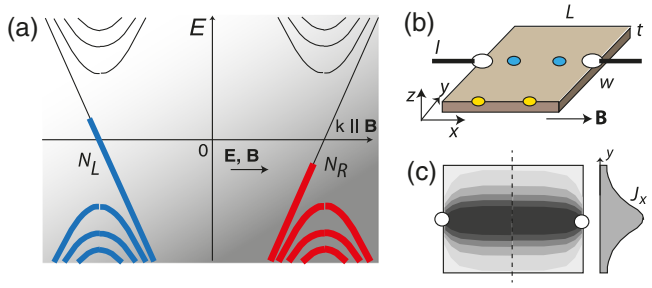

FIG. 1. (a) The Landau spectrum of Weyl fermions. In a field $\mathbf{B}\|\hat{\mathbf{x}}$, the lowest Landau levels are chiral with velocity $\mathbf{v}$ either $\|\mathbf{B}$ or $-\mathbf{B}$. Application of $\mathbf{E}\|\mathbf{B}$ transfers charge between them, which increases the left-moving population N_L at the expense of the right-moving population N_R (the bold blue and red curves indicate occupations of the LLs). Panel (b) shows a pair of voltage contacts (blue dots) placed on the line joining the current contacts (white circles). A second pair (yellow) is placed along an edge. Panel (c) is a schematic drawing of the intensity map of J_x (with dark regions being the most intense) when current-jetting effects are pronounced. The profile of J_x vs y (with x at the dashed line) is sketched on the right.

of N_L and N_R implies that the chiral charge density $\rho^5 = (N_L - N_R)/V$ is conserved, just like the total charge density $\rho_{\rm tot} = (N_L + N_R)/V$ (V is the sample volume). However, application of an electric field $\mathbf{E}\|\mathbf{B}$ breaks the chiral symmetry by inducing mixing between the left- and right-moving branches [Fig. 1(a)] (for a pedagogical discussion, see Ref. [7]). A consequence is that conservation of ρ^5 is violated by a quantity $\mathcal{A}$ called the anomaly term, viz. $\nabla\cdot\mathbf{J}^5 + \partial_t\rho^5 = e\mathcal{A}$, where $\mathbf{J}^5$ is the axial current density. [From the density of states in the LLL and the rate of change $\partial k_z/\partial t$ induced by $\mathbf{E}$, we obtain $\mathcal{A} = (e^2/4\pi^2\hbar^2)\mathbf{E}\cdot\mathbf{B}$.] The presence of $\mathbf{J}^5$ is detected as a large, negative, longitudinal magnetoresistance (LMR). This constitutes the chiral anomaly. (The anomaly first appeared in the theory of π-meson decay [8,9]. See Refs. [10,11].) The conditions for observing the anomaly in Dirac semimetals were discussed, e.g., in Refs. [3,12–15].

In 2015, Xiong *et al.* reported the observation of a fivefold to sixfold suppression of the LMR in Na_3Bi, identified with the chiral anomaly [16]. A year later, Hirschberger *et al.* [17] observed the chiral anomaly, including its thermoelectric signature in the half-Heusler GdPtBi. Although the low-lying states in GdPtBi are not Dirac-like in zero B, the application of a Zeeman field splits both conduction and valence bands to produce protected crossings that define Weyl nodes. With $\mathbf{B}\|\mathbf{E}$, a fivefold LMR was observed with a profile very similar to that in Na_3Bi. In both Na_3Bi and GdPtBi, the carrier mobility is relatively low (3000 and 2000 $\rm cm^2/Vs$ at 2 K, respectively).

There have also been several reports of negative LMR observed in the Weyl semimetals TaAs, NbP, and analogs [18–21]. However, the weakness of their LMR signals (50–100 times weaker than in Na_3Bi) and their fragility with respect to the placement of contacts, together with the high mobilities of the Weyl semimetals (150 000 to 200 000 $\rm cm^2/Vs$), have raised concerns about current-jetting artifacts [20,21]. As a consequence, there is considerable confusion and uncertainties about LMR experiments, in general, and the LMR reported in the Weyl semimetals, in particular. The concerns seem to have spread to Na_3Bi and GdPtBi as well, notwithstanding their much larger LMR signal.

There is good reason for the uncertainties. Among the resistivity matrix elements, measurements of the longitudinal resistivity ρ_{xx} (for $\mathbf{B}\|\hat{\mathbf{x}}$) are the most vulnerable to inhomogeneous flow caused by current jetting. Even when the LMR signal in a sample is mostly intrinsic, the chiral anomaly produces an intrinsic conductivity anisotropy u, which unavoidably produces inhomogeneous current distributions that distort the observed LMR profile. Given the prominent role of LMR in chiral-anomaly investigations, it is highly desirable to understand these effects at a quantitative level and to develop a procedure that removes the distortions.

A major difference between the large LMR systems Na_3Bi and GdPtBi, on the one hand, and the Weyl semimetals, on the other, is their carrier densities. Because the density is low in both Na_3Bi (1×10^{17} $\rm cm^{-3}$) and in GdPtBi (1.5×10^{17} $\rm cm^{-3}$), the field B_Q required to force the chemical potential ζ into the LLL is only 5–6 T. By contrast, B_Q is 7–40 T in the Weyl semimetals. As shown in Fig. 1(a), the physics underlying the anomaly involves the occupation of chiral, massless states. Occupation of the higher LLs (when $B < B_Q$) leads to strong suppression of the anomaly [17]. Moreover, as discussed below, LMR measurements involve a competition between the anomaly mechanism ("the quantum effect") and classical current-jetting effects, which onset at a second field scale $B_{\rm cyc}$. The relative magnitudes of these field scales dictate which effect dominates.

Here, we report a series of experiments designed to separate intrinsic from extrinsic effects in LMR experiments. Focusing of the current density $J(\mathbf{r})$ into a beam strongly reduces its value at the edges of a sample. As shown in Sec. II, the effects of current jetting can be neatly factored into a quantity $\mathcal{L}_y$ (line integral of J_x), which can be measured by local voltage contact pairs. By comparing local voltage drops at the maximum and minimum of the profile of J, we devise a litmus test that sharply distinguishes the two chiral-anomaly semimetals from the case of pure Bi (Sec. III). Adopting a quantitative treatment (Sec. IV), we show how the intrinsic $\rho_{xx}(B)$ can be derived from the local voltage results. Applying this technique to Na_3Bi, we obtain the intrinsic profiles of $\rho_{xx}(B)$ and the anisotropy, with current-jetting distortions removed. The degree of distortion at each B value becomes plainly evident. The competition between the quantum and

classical effects is described in Sec. V. To look beyond Na_3Bi and GdPtBi, we discuss how the tests can be extended using focused ion beam techniques to test $ZrTe_5$, which grows as a narrow ribbon. The Weyl semimetals, e.g., TaAs, require availability of ultrathin films. The planar angular magnetoresistance (Sec. VI) provides a second litmus test—one that is visually direct when displayed as a parametric plot (Sec. VII). In Sec. VIII, we summarize our results.

II. THE SQUEEZE TEST

Current jetting refers to the focusing of the current density $\mathbf{J}(\mathbf{r})$ into a narrow beam $\|\mathbf{B}$ arising from the field-induced anisotropy u of the conductivity (the drift of carriers transverse to $\mathbf{B}$ is suppressed relative to the longitudinal drift). To maximize the gradient of J along the y axis, we select platelike samples with $L,w \gg t$, where w, L, and t are the width, length, and thickness, respectively [Fig. 1(b)]. The x and y axes are aligned with the edges and $\mathbf{B}\|\hat{\mathbf{x}}$. As sketched in Fig. 1(c), the profile of J_x vs y is strongly peaked at the center of the sample and suppressed towards the edges. In the squeeze test, we measure the voltage difference across a pair of contacts (blue dots) along the line joining the current contacts (which we call the spine), as well as that across a pair on the edge (yellow dots). To accentuate current-jetting effects, we keep the current contact diameters d_c small ($d_c \ll w$) and place them on the top face of the sample wherever possible. (The squeeze test cannot be applied to needlelike crystals.)

A. Sample preparation

We provide details on the preparation of Na_3Bi, which is by far the most difficult of the three materials to work with. Na_3Bi crystallizes to form hexagonal platelets with the broad face normal to (001). The crystals investigated here were grown under the same conditions as the samples used in Xiong *et al.* [16]; they have carrier densities 1×10^{17} cm^{-3} and B_Q in the range 5–6 T. These crystals should be distinguished from an earlier batch [22] that have much higher carrier densities (3–6 $\times 10^{19}$ cm^{-3}) for which we estimate $B_Q \sim 100$ T. No evidence for negative LMR was obtained in the highly doped crystals [22].

Because of the high Na content, crystals exposed to ambient air undergo complete oxidation in about 5 s. The stainless growth tubes containing the crystals were opened in an argon glovebox equipped with a stereoscopic microscope, and all sample preparation and mounting were performed within the glovebox. The crystals have the ductility of a soft metal. Using a sharp razor, we cleaved the bulk crystal into platelets 1×1 mm^2 on a side with thickness 100 μm. Current and voltage contacts were painted on using silver paint (Dupont 4922N). A major difficulty was achieving low-resistance contacts on the top face (for measuring R_{spine}). After much experimentation, we found it expedient to remove a thin layer of oxide by lightly sanding with fine emery paper (within the glovebox). The sample was then placed inside a capsule made of G10 epoxy. After sealing the lid with STYCAST epoxy, the capsule was transferred to the cryostat.

We contrast two cases. In case 1, the anisotropy $u = \sigma_{xx}/\sigma_{yy}$ increases in a longitudinal field $\mathbf{B}$ because the transverse conductivity σ_{yy} decreases steeply (as a result of cyclotronic motion), while σ_{xx} is unchanged in B. With $\mathbf{B}\|\hat{\mathbf{x}}$, the two-band model gives the resistivity matrix

$$\tilde{\rho}(B) = \begin{bmatrix} [\sigma_e + \sigma_h]^{-1} & 0 \\ 0 & [\frac{\sigma_e}{\Delta_e} + \frac{\sigma_h}{\Delta_h}]^{-1} \end{bmatrix} \quad (1)$$

(we suppress the z component for simplicity). The zero-B conductivities of the electron and hole pockets are given by $\sigma_e = ne\mu_e$ and $\sigma_h = pe\mu_h$, with n and p the electron and hole densities, respectively, and e the elemental charge. Note that μ_e and μ_h are the mobilities in the electron and hole pockets, respectively, and $\Delta_e = (1 + \mu_e^2 B^2)$ and $\Delta_h = (1 + \mu_h^2 B^2)$. With $\mathbf{B}\|\hat{\mathbf{x}}$, the off-diagonal elements vanish. In case 1, we assume that σ_e and σ_h remain constant. Hence, the observed resistivity ρ_{xx} is unchanged in B. However, the transverse conductivity σ_{yy} decreases (as $1/B^2$ in high B). The anisotropy arises solely from the suppression of the conduction transverse to $\mathbf{B}$ by the cyclotron motion of both species of carriers.

Case 2 is the chiral anomaly regime in the Dirac semimetal. Charge pumping between Landau levels (LLs) of opposite chirality leads to an axial current that causes σ_{xx} to increase with B. Simultaneously, the 1D nature of the LL dispersion suppresses the transverse conductivity σ_{yy}. Hence, the increase in u derives equally from the opposite trends in σ_{xx} and σ_{yy}.

Denoting field-induced changes by Δ, we have

$$\text{Case 1}: \ \Delta u > 0 \Leftrightarrow \Delta\sigma_{xx} \sim 0; \Delta\sigma_{yy} < 0, \quad (2)$$

$$\text{Case 2}: \ \Delta u > 0 \Leftrightarrow \Delta\sigma_{xx} > 0; \Delta\sigma_{yy} < 0. \quad (3)$$

In the test, the voltage drops V_{spine} and V_{edge} are given by

$$V_{\text{edge}}(B) = -\rho_{xx}(B) \int_0^{\ell} J_x(x, w/2; B)dx \equiv \rho_{xx}\mathcal{L}_e, \quad (4)$$

$$V_{\text{spine}}(B) = -\rho_{xx}(B) \int_0^{\ell} J_x(x, 0; B)dx \equiv \rho_{xx}\mathcal{L}_s, \quad (5)$$

where $\mathcal{L}_e(B)$ and $\mathcal{L}_s(B)$ are the line integrals of J_x along the edge and spine, respectively (ℓ is the spacing between voltage contacts). The intrinsic B dependence [expressed in $\rho_{xx}(B)$] has been cleanly separated from the extrinsic B dependence of $\mathcal{L}_e(B)$ and $\mathcal{L}_a(B)$, which arises from current focusing effects.

The area under the curve of J_x vs y is conserved, i.e.,

$$\int_{w/2}^{w/2} J_x(x,y;B)dy = I, \tag{6}$$

with I the applied current. At $B=0$, we may take $\mathbf{J}$ to be uniform with the magnitude $J_0 = I/(wt)$. The line integral reduces to $\mathcal{L}_0 = J_0\ell$. In finite B, focusing of the current beam implies that the current density is maximum along the spine and minimum at the edge, i.e., $J_x(x,0;B) > J_x(x,w/2;B)$. Moreover, Eq. (6) implies that $J_x(x,0;B) > J_0 > J_x(x,w/2;B)$. Hence, the line integrals satisfy the inequalities

$$\mathcal{L}_s(B) > \mathcal{L}_0 > \mathcal{L}_e(B). \tag{7}$$

If both σ_e and σ_h are B independent, as in case 1, we have from Eqs. (4), (5), and (8),

$$V_{\text{spine}}(B) > V_0 > V_{\text{edge}}(B), \tag{8}$$

where V_0 is the voltage drop across both pairs at $B=0$. Clearly, V_{spine} increases monotonically with B, while V_{edge} decreases. Physically, focusing the current density along the spine increases the local E field there. Current conservation then requires J_x to be proportionately suppressed along the edges. Measuring V_{edge} alone yields a negative LMR that is spurious.

In case 2, however, ρ_{xx} decreases intrinsically with B because of the chiral anomaly, while $\mathcal{L}_s$ increases. Competition between the two trends is explicitly seen in the profile of V_{spine} vs B. As shown below, in Na_3Bi and GdPtBi, the intrinsic decrease in ρ_{xx} dominates, so both V_{spine} and V_{edge} decrease with B. We remark that, from Eq. (8), V_{spine} always lies above V_{edge}. Moreover, when the rate of increase in $\mathcal{L}_s$ begins to exceed (in the absolute sense) the rate of decrease in ρ_{xx} at sufficiently large B, the curve of $V_{\text{spine}}(B)$ can display a broad minimum above which V_{spine} increases.

Hence, if both V_{spine} and V_{edge} are observed to decrease with increasing B, the squeeze test provides positive confirmation that the observed LMR is intrinsic. Their field profiles bracket the intrinsic behavior of ρ_{xx}. Conversely, if intrinsic LMR is absent (i.e., σ_{xx} is unchanged), V_{spine} and V_{edge} display opposite trends (the marginal case when the intrinsic LMR is weak is discussed in Sec. IV).

We remark that the current-jetting effects cannot be eliminated by using very small samples (e.g., using nanolithography). As long as we remain in the classical transport regime, the equations determining the functional form of $J(x,y)$ in strong B are scale invariant. Because intrinsic length scales (e.g., the magnetic length ℓ_B or the skin depth δ_s) are absent in classical dc transport, the same flow pattern is obtained on either mm or micron-length scales.

III. RESULTS OF SQUEEZE TEST

The results of applying the squeeze test on the three systems are summarized in Fig. 2. In panels (a) and (b), we show the voltage drops V_{edge} and V_{spine} measured in pure bismuth (sample B1). The signals are expressed as the effective resistances

$$R_{\text{edge}} = \rho_{xx}(B).\mathcal{L}_e(B)/I, \tag{9}$$

$$R_{\text{spine}} = \rho_{xx}(B).\mathcal{L}_s(B)/I. \tag{10}$$

The steep decrease in R_{edge} [panel (a)] illustrates how an apparent but spurious LMR can easily appear when the mobility is very high (in Bi, μ_e exceeds 10^6 cm^2/Vs at 4 K). Comparison of R_{edge} and R_{spine} measured simultaneously shows that they have opposite trends vs B. As σ_e and σ_h are obviously B independent in Bi, ρ_{xx} is also B independent. By Eqs. (9) and (10), the changes arise solely from $\mathcal{L}_e$ and $\mathcal{L}_s$. Hence, Figs. 2(a) and 2(b) verify experimentally that V_{edge} and V_{spine} display the predicted large variations of opposite signs when current jetting is the sole mechanism present (see simulations in Sec. IV).

Next, we consider Na_3Bi. In this sample (N1), R_{edge} below 20 K decreases by a factor of 50 between $B=0$ and 10 T [Fig. 2(c)]. This is an order of magnitude larger than observed in Ref. [16]. The increase arises from the enhanced current focusing effect in the present contact placement utilizing small current contacts attached to the broad face of the crystal, as well as a larger u. In spite of the enhanced jetting, R_{spine} shows a pronounced decrease in contrast to the case for Bi. The intrinsic decrease in ρ_{xx} dominates the increase in $\mathcal{L}_s$ throughout [see Eq. (10)]. Hence, we conclude that there exists a large intrinsic, negative LMR that forces R_{spine} to decrease, despite the focusing of $J(\mathbf{r})$ along the ridge. Further evidence for the competing scenario comes from the weak minimum at 10 T in the curves below 40 K in Fig. 2(d). As anticipated above, in large B, ρ_{xx} approaches a constant because of the saturation chiral-anomaly term. However, $\mathcal{L}_s$ continues to increase because the transverse conductance worsens. Consequently, R_{spine} goes through a minimum before increasing. This is seen in R_{spine} but absent in R_{edge}.

A feature that we currently do not understand is the large V-shaped cusp in weak B. At 100 K, the cusp is prominent in V_{spine} but absent in V_{edge}.

In Figs. 2(e) and 2(f), we show the field profiles of R_{edge} and R_{spine} measured in GdPtBi (sample G1). Again, as in Na_3Bi, the anomaly-induced decrease in ρ_{xx} dominates the increase in $\mathcal{L}_s$, and R_{spine} is observed to decrease in increasing B. The relative decrease in R_{edge} is larger than that in R_{spine}. Further, R_{spine} below 10 K shows the onset of a broad minimum above 10 T [Fig. 2(f)], whereas R_{edge} continues to fall.

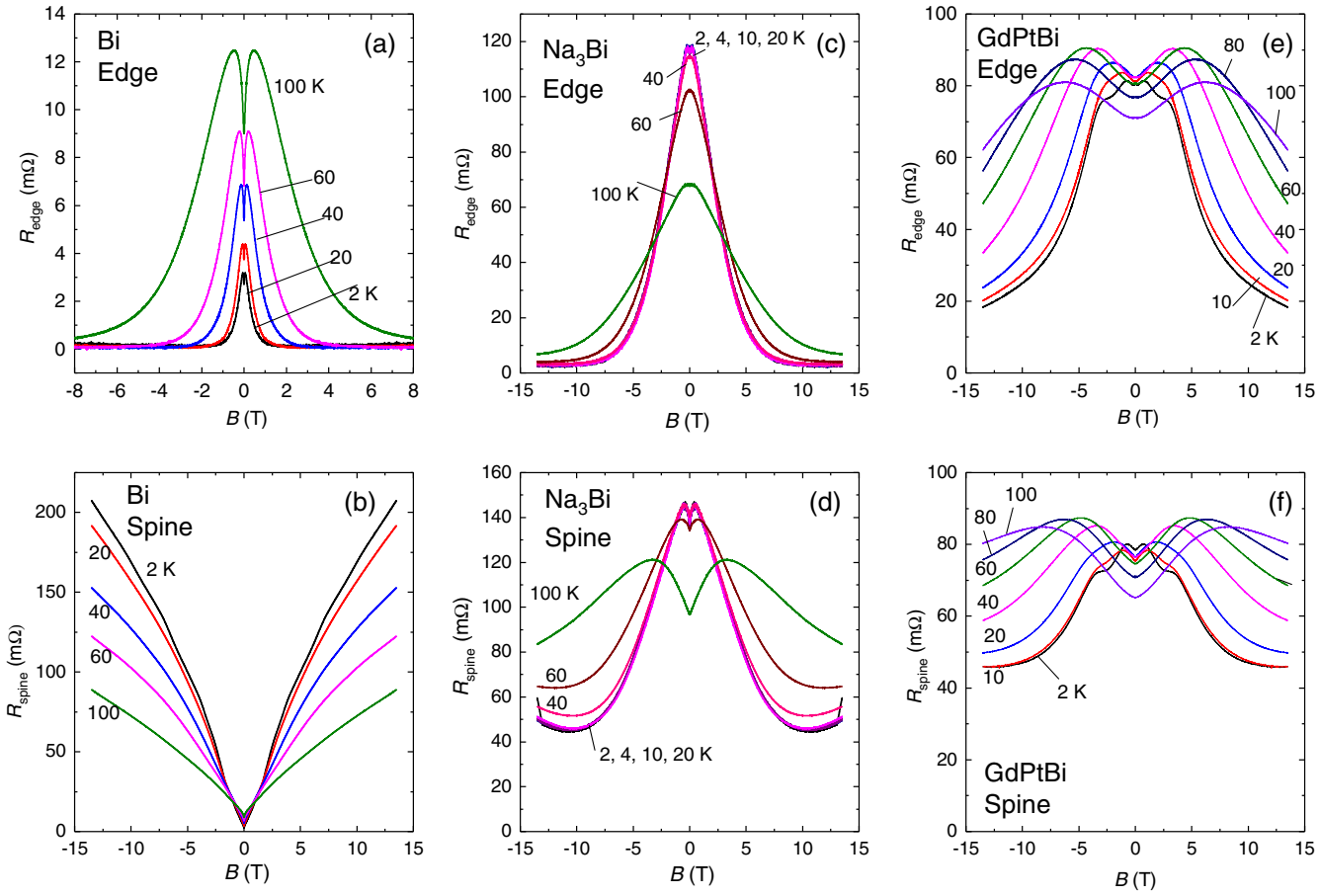

FIG. 2. Comparison of squeeze-test results in pure bismuth (case 1) and in Na_3Bi and GdPtBi (case 2). Panels (a) and (b) display the voltage drops V_{edge} and V_{spine} (expressed as R_{edge} and R_{spine}, respectively) measured in Bi (sample B1). In panel (a), R_{edge} displays a steep decrease with increasing B that steepens as T decreases from 100 K to 2 K. By contrast, R_{spine} increases steeply. The opposite trends in (a) and (b) imply that both arise from pure current jetting, strictly reflecting changes in $\mathcal{L}_e$ and $\mathcal{L}_s$, respectively [Eqs. (9) and (10)]. By contrast, in Na_3Bi (sample N1), both R_{edge} decrease with B [panels (c) and (d), respectively]. This implies that $\rho_{xx}(B)$ decreases uniformly throughout the sample. Nonetheless, current focusing effects (expressed by $\mathcal{L}_e$ and $\mathcal{L}_s$) are visible. Below 20 K, $\mathcal{L}_e$ exaggerates the decrease in R_{edge}, while $\mathcal{L}_s$ counters some of the intrinsic decrease in R_{spine}. A telling feature is the weak upturn in R_{spine} above 10 T. When the intrinsic LMR is saturated, $\mathcal{L}_s$ produces a weak increase in R_{spine}. In GdPtBi [sample G1, panels (e) and (f)], both R_{edge} and R_{spine} also decrease with increasing B. Below 10 K, the decrease in R_{edge} is much larger than that in R_{spine}. The latter also attains a broad minimum above 10 T (but not the former). These features confirm that $\mathcal{L}_e$ amplifies the growth in the intrinsic LMR, while $\mathcal{L}_s$ partially counters it.

These features, in accordance with the discussion above, are amenable to a quantitative analysis that yields the intrinsic field profiles of both ρ_{xx} and u (Sec. IV).

IV. THE INTRINSIC LMR PROFILE

The factorization expressed in Eqs. (9) and (10) allows us to obtain the intrinsic field profile of $\rho_{xx}(B)$ in the face of strong current-density inhomogeneity induced by jetting. To start, we note that, once the boundaries are fixed, the functional form of the inhomogeneous current density $\mathbf{J}(\mathbf{r})$ depends only on the conductivity anisotropy u regardless of its microscopic origin. Assuming a constant $\rho_{xx} = \rho_0$ (i.e., case 1), we first calculate, by numerical simulation, the effective resistances $R^0_{edge}(u)$ and $R^0_{spine}(u)$ over a broad range of u. For simplicity, the simulation is performed for a sample in the 2D limit by solving the anisotropic Laplace equation

$$[\sigma_{xx}\partial_x^2 + \sigma_{yy}\partial_y^2]\psi(x,y) = 0 \tag{11}$$

for the potential $\psi(x,y)$ at selected values of u. We used the relaxation method on a triangular mesh with Dirichlet boundary conditions at the current contacts [inset in Fig. 3(a)].

Figure 3(a) displays the calculated curves of R^0_{edge} and R^0_{spine} in a 2D sample with the aspect ratio matched to that in the experiment on Na_3Bi. As expected, with ρ_{xx} set to a constant, the two curves diverge. This reflects the

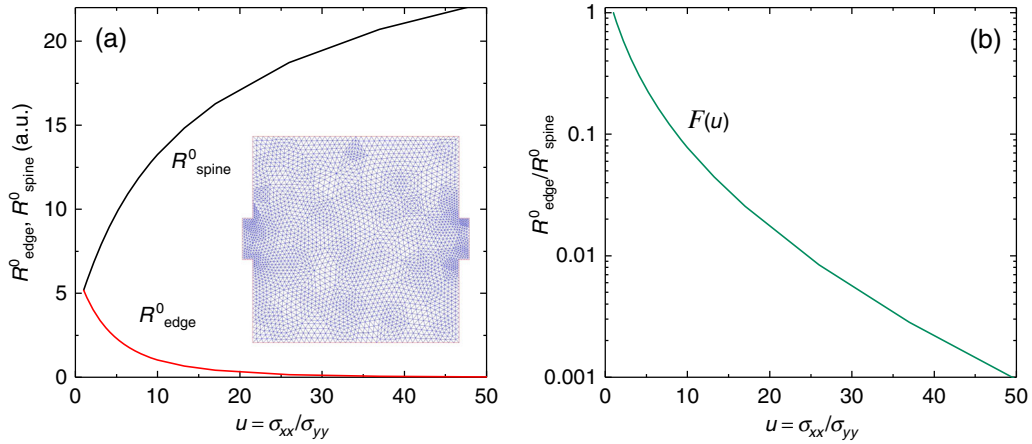

FIG. 3. Procedure to obtain the intrinsic LMR curve $R_{\rm intr}$ vs B and the intrinsic anisotropy $u = \rho_{yy}/\rho_{xx}$ from measurements of $R_{\rm edge}$ and $R_{\rm spine}$. Panel (a) plots the calculated resistances $R^0_{\rm edge}$ and $R^0_{\rm spine}$ vs u with $\rho_{xx} = \rho_0$ (case 1) [obtained by solving the anisotropic Laplace equation (11)] in a 2D sample (matched to x and y dimensions of the sample). The divergent trends reflect the enhancement of $J(\mathbf{r})$ along the spine and its decrease at the edge. The inset shows the triangulation network generated during the simulation. The stubs on the left and right edges are current contacts. Panel (b) plots the calculated template function $\mathcal{F}(u)$ in the semilog scale [Eq. (12)]. Equating the measured ratio $\mathcal{G}(B)$ to $\mathcal{F}(u)$, and using Eq. (13), we derive the intrinsic field profiles of $R_{\rm intr}$ and u (see Fig. 4).

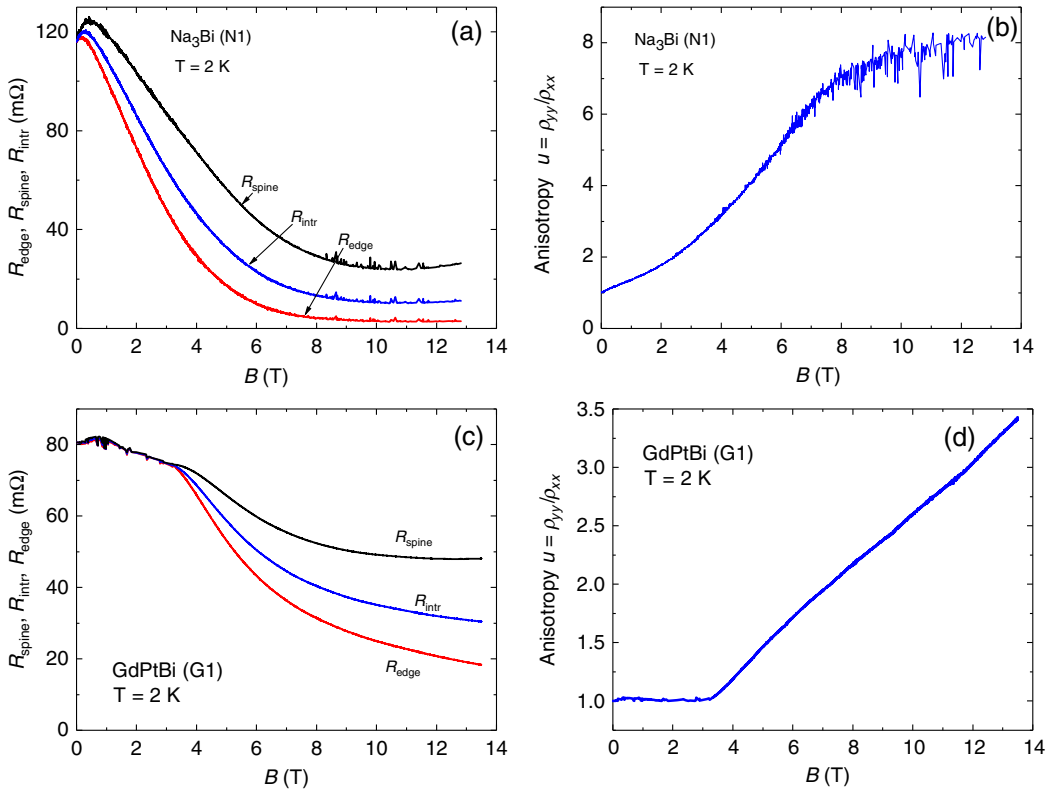

FIG. 4. The intrinsic field profiles of $\rho_{xx}(B)$ and anisotropy $u(B)$ derived by applying Eqs. (12)–(14). Panel (a) shows the curves of $R_{\rm spine}$ (black) and $R_{\rm edge}$ (red) measured in Na_3Bi at 2 K. The inferred intrinsic profile $R_{\rm intr}$ (blue curve) is sandwiched between the measured curves. In this sample (N1), $R_{\rm intr}$ decreases by a factor of 10.9 between $B = 0$ and 10 T. We note that $R_{\rm spine}$ displays a weak minimum near 10 T, which results from the competing trends in $\rho_{xx}(B)$ and $\mathcal{L}_s(B)$. Panel (b) displays the intrinsic $u(B)$ in Na_3Bi derived from Eq. (13). The corresponding curves for GdPtBi (sample G1 at 2 K) are shown in panels (c) and (d). Again, $R_{\rm intr}(B)$ in panel (c) is sandwiched between the curves of $R_{\rm edge}(B)$ and $R_{\rm spine}(B)$. Panel (d) plots the intrinsic anisotropy $u(B)$. In GdPtBi, the Weyl nodes only appear when B is strong enough to force band crossing. In G1, this occurs at 3.4 T (u remains close to 1 below this field).

simultaneous enhancement of the E field along the spine and its steep decrease at the edge caused by pure current jetting.

From the calculated resistances, we form the ratio

$$\mathcal{F}(u) = R^0_{\rm edge}/R^0_{\rm spine} = \mathcal{L}_e/\mathcal{L}_s. \tag{12}$$

The template curve $\mathcal{F}(u)$, which depends only on u, is plotted in semilog scale in Fig. 3(b).

Turning to the values of $R_{\rm edge}(B)$ and $R_{\rm spine}(B)$ measured in Na_3Bi at the field B, we form the ratio $\mathcal{G}(B) = R_{\rm edge}/R_{\rm spine} = \mathcal{L}_e/\mathcal{L}_s$. Although $\mathcal{G}$ is implicitly a function of u, it is experimentally determined as a function of B (how u varies with B is not yet known). We remark that $\mathcal{G}(B)$ and $\mathcal{F}(u)$ represent the same physical quantity expressed as functions of different variables. To find u, we equate $\mathcal{G}(B)$ to $\mathcal{F}(u)$ in the template curve. This process leads to the equation

$$u(B) = \mathcal{F}^{-1}(\mathcal{G}(B)), \tag{13}$$

from which we determine u given B. Finally, because $R^0_{\rm edge}$ and $R^0_{\rm spine}$ are known from the simulation, we obtain the intrinsic profile of ρ_{xx} as a function of B using the relations

$$\rho_{xx}(B) = \frac{R_{\rm edge}(B)}{R^0_{\rm edge}(u)}\rho_0 = \frac{R_{\rm spine}(B)}{R^0_{\rm spine}(u)}\rho_0. \tag{14}$$

The redundancy (either resistance may be used) provides a useful check for errors in the analysis.

The results of the analysis are shown in Fig. 4 for both Na_3Bi and GdPtBi. In Fig. 4(a), we plot $\rho_{xx}(B)$ in Na_3Bi [as the intrinsic curve $R_{\rm intr}(B)$, in blue]. As expected, $R_{\rm intr}(B)$ is sandwiched between the measured curves of $R_{\rm edge}(B)$ and $R_{\rm spine}(B)$. The field profile of the intrinsic anisotropy u is displayed in Fig. 4(b). It is interesting to note that, in Na_3Bi at 2 K, the intrinsic conductivity anisotropy increases to 8 as B is increased to 14 T. This engenders significant distortion of $\mathbf{J}(\mathbf{r})$ away from uniform flow. The analysis provides a quantitative measure of how current-jetting effects distort the measurements. At 10 T, $R_{\rm spine}$ is larger than $R_{\rm intr}$ by a factor of 2.3, whereas $R_{\rm edge}$ is 4.0 times smaller than $R_{\rm intr}$. The plots show explicitly how $R_{\rm spine}(B)$ still decreases (by a factor of about 5) between $B = 0$ and 10 T, despite the enhancement in $\mathcal{L}_s$ caused by current jetting. Here, we see explicitly that this occurs because the intrinsic LMR is so large (decreasing by a factor of 10.9 between 0 and 10 T) that the current squeezing factor is always subdominant. With the procedure described, this subdominant distortion can be removed entirely. The corresponding profiles of $\rho_{xx}(B)$ and $u(B)$ in GdPtBi are shown in Figs. 4(c) and 4(d), respectively. Unlike the case in Na_3Bi, a finite B is required to create the Weyl nodes. This occurs at about 3.4 T in G1. Below this field, the system is isotropic (u close to 1).

V. QUANTUM VS CLASSICAL EFFECTS

From the experimental viewpoint, it is helpful to view the LMR experiment as a competition between the intrinsic anomaly-induced decrease in ρ_{xx} (a quantum effect) and the distortions engendered by current jetting (classical effect). To observe a large, negative LMR induced by the chiral anomaly, it is imperative to have the chemical potential ζ enter the LLL. The field at which this occurs, which we call B_Q, sets the onset field for this quantum effect. By contrast, the distortions to $\mathbf{J}$ caused by current jetting onset at the field $B_{\rm cyc}$, which is set by the inverse mobility $1/\mu$. We write $B_{\rm cyc} = \mathcal{A}/\mu$, where the dimensionless parameter $\mathcal{A} = 5$–10, based on the numerical simulations [Eqs. (12) and (13)].

If $B_Q < B_{\rm cyc}$, the LLL is accessed before classical current distortion appears in increasing B. This is the situation in the upper shaded region in the B_Q vs $B_{\rm cyc}$ space in Fig. 5(a). The conditions are favorable for observing the chiral anomaly without worrying about classical current jetting. (To be sure, the chiral anomaly itself leads to a large anisotropy σ_{xx}/σ_{yy} that can distort $\mathbf{J}$. However, this is a quantum effect that follows from the chiral anomaly and can be compensated for.) The measured curves of $R_{\rm spine}$ and $R_{\rm edge}$ bracket the intrinsic ρ_{xx}, which allows the latter to be obtained, as explained in Eqs. (12)–(14). In both Na_3Bi and GdPtBi, $B_Q \sim 5$–6 T, whereas $B_{\rm cyc}$ exceeds 30 T. They fall safely within the shaded area.

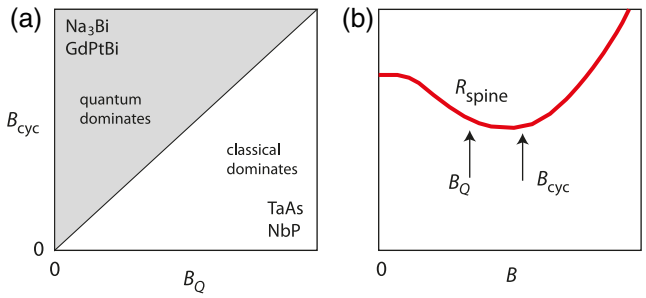

FIG. 5. Competition between the intrinsic chiral-anomaly LMR (with onset field B_Q) and the extrinsic classical effect of current jetting (onset field $B_{\rm cyc} = \mathcal{A}/\mu$, $\mathcal{A} = 5$–10). Panel (a): In the shaded upper-half region, the system enters the LLL before the current-jetting effects dominate as B increases ($B_Q < B_{\rm cyc}$). Panel (b) shows a hypothetical case close to the boundary $B_Q \simeq B_{\rm cyc}$. In the profile of $R_{\rm spine}$, an initial decrease is followed by a steep increase above $B_{\rm cyc}$. For systems in the unshaded region ($B_Q > B_{\rm cyc}$), the LLL is entered long after current-jetting effects become dominant. The classical effect effectively screens the quantum behavior. Bulk crystals of Na_3Bi and GdPtBi fall safely in the upper half, whereas TaAs and NbAs fall in the lower half. One way to avoid current jetting in the latter is to lower B_Q by gating ultrathin-film samples.

As B_Q approaches B_{cyc} [the diagonal boundary in Fig. 5(a)], classical current jetting becomes increasingly problematical. In Fig. 5(b), the schematic curve illustrates the trend of how the quantum behavior can be swamped by the onset of current jetting.

Finally, if $B_Q \gg B_{cyc}$, classical distortion effects onset long before the LLL is accessed. In this case, R_{spine} and R_{edge} display divergent trends vs B. Even if an intrinsic LMR exists, we are unable to observe it in the face of the dominant (artifactual) change in V_{xx} caused by classical current jetting. In the Weyl semimetals TaAs and NbAs, $B_Q \simeq 7$ and 40 T, respectively, whereas $B_{cyc} \sim 0.4$ T (because of their high mobilities). This makes LMR an unreliable tool for establishing the chiral anomaly in the Weyl semimetals. We illustrate the difficulties with R_{edge} and R_{spine} measured in TaAs [Fig. 6(a)] and in NbAs [Fig. 6(b)].

In the initial reports, a weak LMR feature (5%–10% overall decrease) was observed in TaAs and identified with the chiral anomaly. Subsequently, several groups found that both the magnitude and sign of the LMR feature are highly sensitive to voltage contact placement. We can, in fact, amplify the negative LMR to nearly 100%. To apply the squeeze test, we have polished a crystal of TaAs to the form of a thin square plate and mounted contacts in the configuration sketched in Fig. 1(b), with small current contacts (about 80 μm). As shown in Fig. 6(a), R_{edge} at 4 K (thick blue curve) displays a steep decrease, falling to a value approaching our limit of resolution at 7 T. Simultaneously, however, R_{spine} (red) increases rapidly. The two profiles are categorically distinct from those in Na_3Bi and GdPtBi [Figs. 2(c)–2(f)] but very similar to the curves for Bi [Figs. 2(a) and 2(b)]. Moreover, the weak SdH oscillations fix the field B_Q needed to access the LLL at 7.04 T [inset in (a)]. Since $1/\mu \sim 0.06$ T, we infer that the classical current-jetting effect onsets long before the quantum limit is accessed. Hence, TaAs is deep in the right-bottom corner of the phase diagram in Fig. 5(a). The current-jetting effects appear well before TaAs attains the quantum limit at B_Q, and it completely precludes the chiral anomaly from being observed by LMR.

Applying the squeeze test to NbAs next, we display the curves of R_{edge} (black) and R_{spine} (red) at 4 K in Fig. 6(b). Here, both R_{edge} and R_{spine} increase with B, but R_{spine} increases 100 times faster (in the field interval $0 < B <$ 8.5 T, R_{edge} doubles but R_{spine} increases by a factor of 280). The vast difference in the rate of change is direct evidence for the squeezing of $J(\mathbf{r})$ along the spine, as depicted in Fig. 1(c). Again, with $B_Q \sim 40$ T, we infer that NbAs falls deep in the right-bottom corner of Fig. 5(a). Classical current jetting dominates the LMR.

It is worth remarking that the squeeze-test results do not invalidate the ARPES evidence, showing that TaAs and

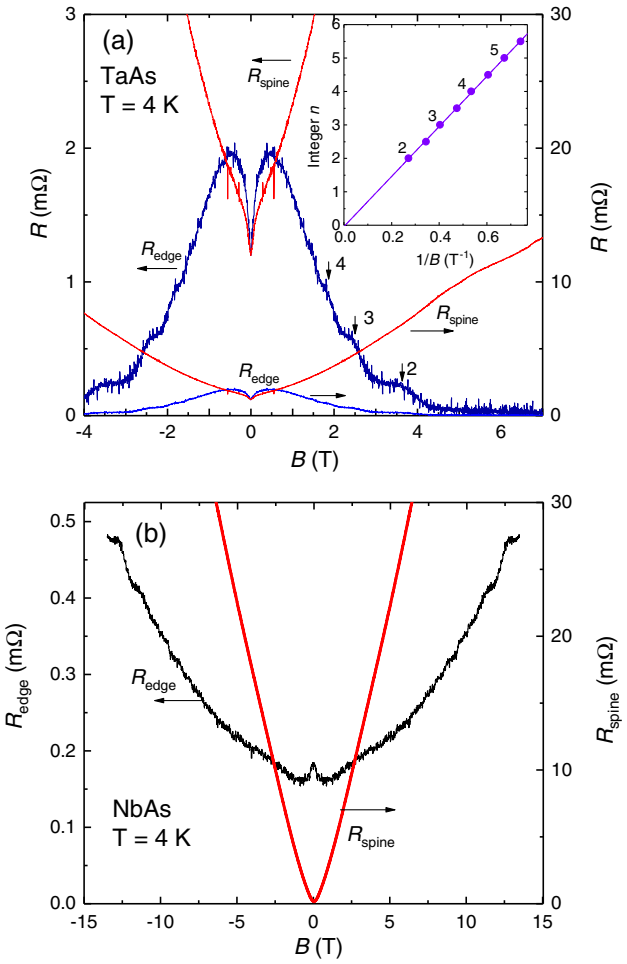

FIG. 6. The squeeze test applied to the Weyl semimetals TaAs and NbAs. Panel (a) shows field profiles of R_{edge} and R_{spine} in TaAs (measured at 4 K) in an in-plane, longitudinal **B** along the "spine" of the sample. The crystal is a thin plate of dimension $2.0 \times 1.5 \times 0.2$ mm^3 with spacing ℓ between voltage contacts of 1.5 mm, and current-contact diameters $d_c \sim 80$ μm. Between 0.5 T and 6 T, R_{edge} (thick blue curve, left axis) is observed to decrease by a factor of about 50 to values below our resolution. However, the spine resistance R_{spine} (red curve) increases by a factor of 7.8 (the right axis replots R_{spine} and R_{edge} reduced by a factor of 10). This implies that the pronounced decrease in R_{edge} is an artifact caused by current jetting, just as observed in pure Bi. The Landau level indices n of the weak SdH oscillations are indicated by vertical arrows. The index plot (inset) shows that $n = 1$ is reached at $B_Q = 7.04$ T, whereas $1/\mu \sim 0.06$ T. Panel (b) shows field profiles of R_{edge} (black curve, left axis) and R_{spine} (red curve, right axis) measured in NbAs at 4 K in longitudinal **B** (crystal size $1.5 \times 1.0 \times 0.4$ mm^3). The small negative LMR anomaly near zero B in R_{edge} has been invoked as evidence for the chiral anomaly even though R_{edge} increases above 1.2 T. By contrast, R_{spine} increases monotonically at a very steep rate (note the difference in vertical scales). In both high-mobility semimetals, classical current-jetting effects onset near 0.4 T, well below B_Q. This makes the chiral anomaly virtually unobservable by LMR.

NbAs are Weyl semimetals. Rather, they demonstrate that the negative LMR results reported to date in the Weyl semimetals fall deep in the regime where classical current-jetting effects dominate.

Figure 5(a) suggests a way to avoid the screening effect of current jetting for the Weyl semimetals. By growing ultrathin films, one may use gating to lower ζ towards zero in the Weyl nodes. This allows the LLL to be accessed at a much lower B_Q. Simultaneously, the increased surface scattering of the carriers will reduce μ (hence increase $B_{\rm cyc}$). By allowing the quantum effect to onset before the classical effect becomes dominant, both trends shift the "operating point" towards the shaded region $B_Q < B_{\rm cyc}$. The ability to tune B_Q by gating will enable more tests for mapping out the current density distribution. The squeeze test is actually easier to implement using thin-film samples. Because several groups worldwide are attempting to grow thin-film TaAs and NbAs, the prospects for the Weyl semimetals seem quite encouraging.

A fourth candidate for the chiral anomaly is $ZrTe_5$ [23,24], which displays a moderately large negative LMR signal (ρ_{xx} decreases by 35%). A very recent experiment [24] has detected a (true) planar Hall effect when the chiral anomaly appears. This implies the simultaneous appearance of a large Berry curvature in applied **B**. However, currently available bulk crystals have a narrow ribbonlike morphology unsuited for the squeeze test (a platelike shape is optimal). However, using focused ion beam (FIB) techniques, we may envisage sculpting the ribbons into thin plates. Microlithography techniques can then be harnessed to deposit voltage contacts for measuring $R_{\rm spine}$ and $R_{\rm edge}$. We are not aware of any technical barrier that would preclude applying the squeeze test on platelike crystals tens of μm on a side. The field profiles of $R_{\rm spine}$ and $R_{\rm edge}$ may then be compared as reported here in both Na_3Bi and GdPtBi. The FIB technique can be applied to future chiral-anomaly candidate materials that do not readily grow as large crystals.

VI. PLANAR ANGULAR MAGNETORESISTANCE

As shown in Eqs. (2) and (3), the growth of the anisotropy u arises differently in cases 1 and 2. The difference leaves a strong imprint on the planar angular magnetoresistance (AMR), which we describe here. In an AMR experiment, **B** is rotated within the x-y plane, while the longitudinal and transverse voltages are recorded. AMR experiments have been used to investigate the resistivity anisotropy produced by the magnetization **M** in ferromagnetic thin films. Recently, Burkov [25] has suggested that AMR measurements may be used to probe the chiral anomaly.

The sample geometry is as defined above but now with broad current contacts and a pair of standard Hall contacts spaced along y [see inset in Fig. 7(b)]. The lab frame (x and y axes) remain fixed to the sides of the sample. The in-plane **B** determines the sample's orthogonal frame **a**, **b**, and **c** (**a**$\|$**B** is tilted at an angle θ relative to $\hat{\mathbf{x}}$ with **c**$\|\hat{\mathbf{z}}$). The tilt produces potential drops V_{xx} and V_{yx} given by

$$V_{xx}/I = \rho_{bb} + \Delta\rho\cos^2\theta, \tag{15}$$

$$V_{yx}/I = \Delta\rho\sin\theta\cos\theta, \tag{16}$$

where ρ_{aa} and ρ_{bb} are the resistivities measured along axes a and b, respectively, and $\Delta\rho = \rho_{aa} - \rho_{bb}$.

By convention, the transverse voltage V_{yx} is dubbed the "planar Hall effect" even though it is strictly even in **B**. As V_{yx} does not satisfy the Onsager relation for a true Hall response, this is a misnomer. [In topological matter, the Berry curvature can generate a true in-plane Hall signal that is odd in **B** and distinct from V_{yx} in Eq. (16).] To avoid confusion, we call V_{yx} the off-diagonal AMR signal and V_{xx} the longitudinal AMR signal.

Generally, the AMR results are not very informative (the same angular pattern is obtained regardless of the microscopic origin of the anisotropy). However, for our problem, we find that the parametric plot of V_{yx} vs V_{xx} provides a litmus test that distinguishes case 1 from case 2.

In case 1, with $\theta = 0$ (**B**$\|\hat{\mathbf{x}}$), V_{xx} detects $\rho_{aa}\mathcal{L}_e$; its "spurious" decrease as B increases arises entirely from $\mathcal{L}_s$. In the orthogonal situation $\theta = \pi/2$, V_{xx} detects $\rho_{bb}\mathcal{L}_0$ (i.e., beam focusing effects are absent). By juxtaposition, the two measurements reveal how u behaves [see Eq. (2)]. This is best shown by plotting V_{yx} against V_{xx}, with θ as the running parameter at a fixed value of the magnitude B. In weak B, the contours describe small loops circling the zero-B point. As B increases, they expand dramatically away from the zero-B point in the direction of increasing V_{xx}. This lopsided expansion (resembling a shock wave) reflects the sharp increase in the resistivity ρ_{bb} measured orthogonal to **B** [while ρ_{aa} remains unchanged; see Eq. (1)]. Indeed, from Eq. (1), we have, in the high-B limit,

$$\rho_{bb} \to \frac{(\mu_e\mu_h)^2B^2}{(\sigma_h\mu_e^2 + \sigma_e\mu_h^2)}. \tag{17}$$

Here, ρ_{bb} increases as B^2 without saturation. Hence, in case 1, we expect the caliper of the contours (given by $\Delta\rho$) to expand without limit as B^2.

Case 2 yields a qualitatively different parametric plot. In the chiral anomaly regime, our measurements show that ρ_{aa} (captured by V_{xx} at $\theta = 0$) decreases intrinsically with increasing B, while ρ_{bb} (at $\theta = \pi/2$) increases by roughly the same fraction. The balanced changes lead to closed contours that expand roughly isotropically from the zero-B point. Moreover, the contour calipers $\Delta\rho$ approach saturation at large B.

VII. PARAMETRIC PLOTS

As in Sec. III, we compare the planar angular MR results in the three materials, pure Bi, Na_3Bi, and GdPtBi. Figure 7(a) displays the angular profiles ρ_{xx} vs θ at selected field magnitudes B measured in Bi at 200 K with $\mathbf{J}\|\hat{\mathbf{x}}$. As $\mathbf{B}$ is tilted away from alignment with $\mathbf{J}$ ($\theta = 0$), ρ_{xx} increases very rapidly at a rate that varies nominally as B^2. The overall behavior in ρ_{xx} is a very large increase with B as soon as $|\theta|$ exceeds 10°. However, at $\theta = 0$, a decrease in ρ_{xx} of roughly 50% can be resolved. This is the spurious LMR induced by pure current jetting. The off-diagonal signal ρ_{yx} shows the $\sin\theta.\cos\theta$ variation described in Eq. (16) (ρ_{yx} is strictly even in B).

The corresponding traces of ρ_{xx} and ρ_{yx} measured in Na_3Bi at 2 K are shown in Figs. 7(c) and 7(d), respectively. Although the curves for ρ_{yx} are similar to those in Bi, a qualitatively different behavior in ρ_{xx} becomes apparent. At $\theta = 0$, ρ_{xx} is suppressed by a factor of about 7 (when the chiral anomaly appears). In the transverse direction ($\theta = 90°$), the poor conductance transverse to $\mathbf{B}$ in the LLL raises ρ_{xx} by a factor of about 2.5. In terms of absolute magnitudes, the changes to ρ_{xx} are comparable along the two orthogonal directions, in sharp contrast with the case in Bi. This "balanced" growth leaves a clear imprint in the parametric plots. The off-diagonal signal ρ_{yx} displays the same $\sin\theta.\cos\theta$ variation as in Bi.

The plots of ρ_{xx} and ρ_{yx} for GdPtBi in Figs. 7(e) and 7(f) also show a concentric pattern. A complication in GdPtBi is that the nature of the Weyl node creation in the field (by the Zeeman shift of parabolic touching bands) is anisotropic

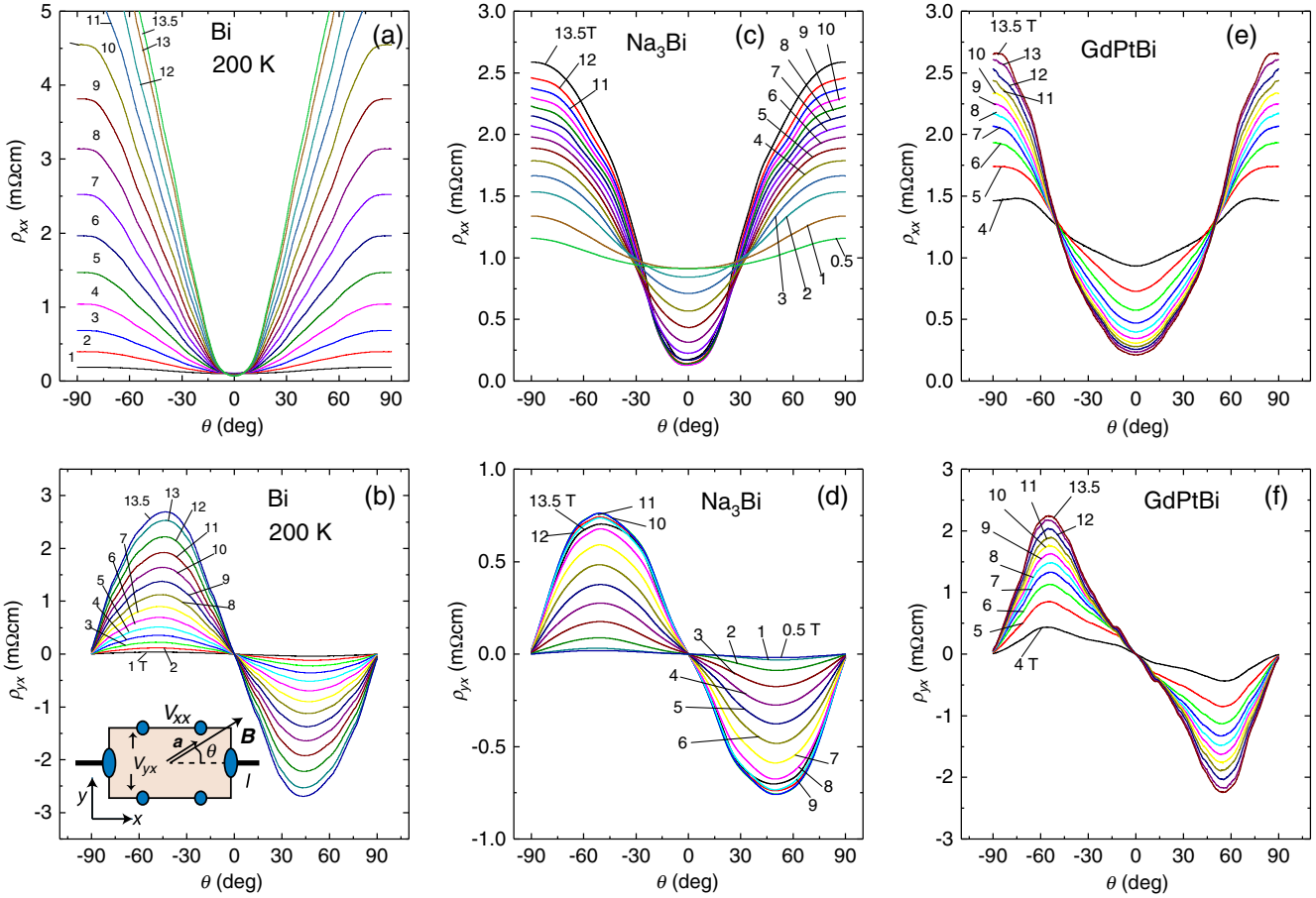

FIG. 7. Planar AMR measurements in Bi, Na_3Bi, and GdPtBi. Panels (a) and (b) show the θ dependence of the diagonal and off-diagonal AMR signals, expressed as effective resistivities ρ_{xx} and ρ_{yx}, respectively, in Bi (sample B2) at 200 K. In panel (a), ρ_{xx} decreases with increasing B when $\theta = 0$ (spurious LMR produced by current jetting). When $|\theta|$ exceeds 20°, ρ_{xx} increases steeply with both $|\theta|$ and B. In absolute terms, the increase in ρ_{xx} at $\theta = 90°$ far exceeds its decrease at $\theta = 0$. The off-diagonal MR ρ_{yx} follows the standard $\sin\theta.\cos\theta$ variation [panel (b)]. Panel (c) shows curves of ρ_{xx} for Na_3Bi (sample N2) at 4 K. The decrease in ρ_{xx} at $\theta = 0$ is roughly comparable with the increase at 90°. A similar balanced pattern is observed in GdPtBi (sample G1) measured at 2 K [panel (e)]. In both case 2 systems, the comparable changes in ρ_{xx} measured at 0° and 90° contrast with the lopsided changes seen in Bi (case 1). The off-diagonal ρ_{yx} in both Na_3Bi and GdPtBi [panels (d) and (f)] show the standard $\sin\theta.\cos\theta$ profile. The profiles in panel (f) are distorted by anisotropic features associated with the creation of the Weyl pockets. The inset in panel (b) shows the sample geometry with $\mathbf{a}\|\mathbf{B}$, both at the tilt angle θ to $\hat{\mathbf{x}}$.

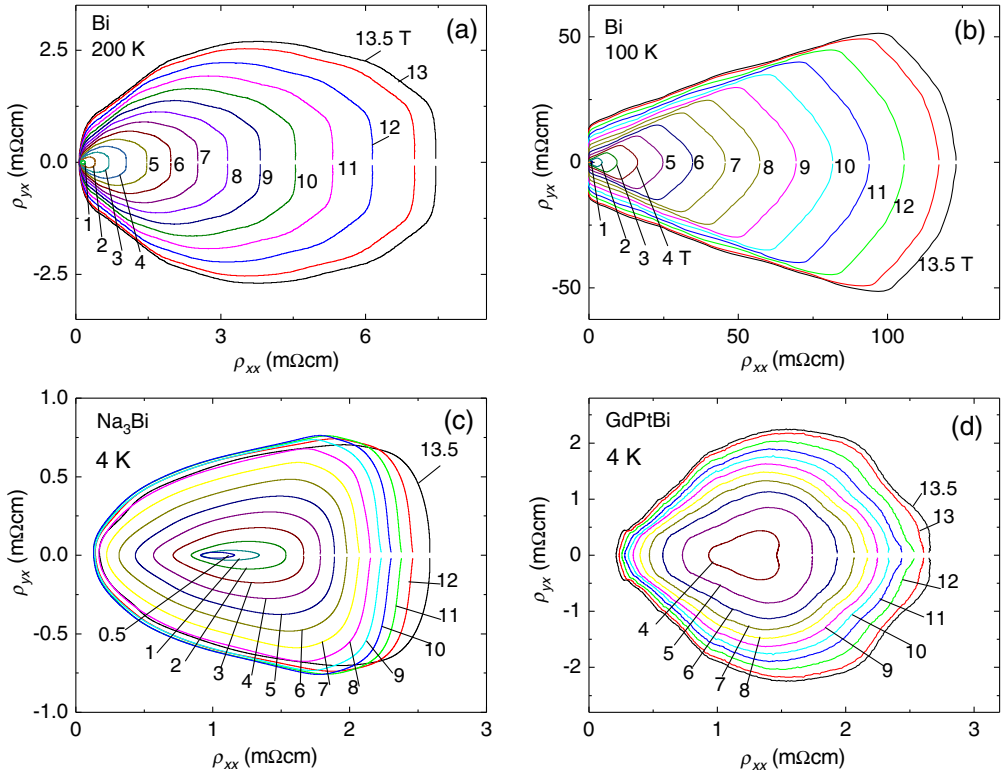

FIG. 8. Parametric plots of the planar AMR signals. Panel (a) shows the orbits in pure Bi at 200 K (sample B2) obtained by plotting ρ_{xx} vs ρ_{yx} with θ as the parameter and with B kept fixed. The orbits start at the left (small ρ_{xx}) and end at the right (large ρ_{xx}). As B increases, the orbits expand without saturation to the right. Panel (b) shows the same plots measured at 100 K. The increased mobility strongly amplifies the lopsided expansion pattern, which resembles a shock wave. The orbits in the parametric plots measured in Na_3Bi (sample N2, at 4 K) and GdPtBi (G1) at 2 K [panels (c) and (d), respectively] are nominally concentric around the point at $B = 0$. The differences between case 1 and case 2 reflect the very different behaviors of ρ_{xx} at the extreme angles $\theta = 0$ and 90°, as discussed in Fig. 7.

(dependent on the direction of **B**). The existence of low-B oscillations adds a modulation to the off-diagonal curves, which distorts the variation from the $\sin\theta.\cos\theta$ form. Nonetheless, a balanced growth in ρ_{xx} is also observed] Fig. 7(e)].

Figure 8 compares the parametric plots in Bi at $T =$ 200 K [panel (a)] and 100 K [panel (b)]. In each orbit (B set at the indicated value), θ starts at 0° on the left limb and ends at 90° on the right. In Fig. 8(a), the steep increase on the right limb causes the orbits to expand strongly to the right. At 100 K [panel (b)], the higher mobility creates exaggerated skewing of the rightward expansion, leading to the emergence of a "shock-wave" pattern. By contrast, the parametric plots in both Na_3Bi [Fig. 8(c) and GdPtBi in panel (d)] show concentric orbits that expand in a balanced pattern as anticipated above. The contrast between case 1 [panels (a) and (b)] and case 2 directly reflects the distinct nature of mechanisms that increase the anisotropy u [see Eqs. (2) and (3)].

VIII. CONCLUDING REMARKS

As mentioned in Sec. I, the existence of a negative LMR that is intrinsic is relatively rare. However, the observation of an artifactual decrease V_{xx} in the LMR geometry is a common experience in high-mobility semimetals. To assist in the task of disentangling the rare intrinsic cases from extrinsic cases (mostly caused by current jetting), we described a test that determines the current-jetting distortions and a procedure for removing them. The squeeze test consists of comparing the effective resistance $R_{\rm spine}$ measured along the spine (line joining current contacts) with that along an edge $R_{\rm edge}$. In pure Bi, $R_{\rm spine}$ increases dramatically with B, while $R_{\rm edge}$ decreases. However, in both Na_3Bi and GdPtBi, both $R_{\rm spine}$ and $R_{\rm edge}$ decrease. Hence, an inspection of the trend in $R_{\rm spine}$ allows case 1 (here Bi) to be distinguished from case 2, the two chiral-anomaly semimetals. From the factorization implicit in Eqs. (9) and (10), we relate the experimental ratio $\mathcal{G}$ to the curve $\mathcal{F}$ obtained by numerical simulation. This enables the intrinsic profiles of both $\rho_{xx}(B)$ and u to be obtained from measurements of $R_{\rm edge}$ and $R_{\rm spine}$. After removal of the distortions, ρ_{xx} is seen to decrease by a large factor (10.9) between $B = 0$ and 10 T, while u increases by 8. (For simplicity, the numerical simulation was done in the 2D limit, which we judge is adequate for flakelike samples. Obviously, this can be improved by adopting a fully 3D

simulation.) The yes or no nature of the test based on inspection of R_{spine}, bolstered by the quantitative analysis that removes the subdominant corrections, adds considerable confidence that the chiral-anomaly LMR profiles in Na_3Bi and GdPtBi are intrinsic. Moreover, the subdominant distortion factors arising from current jetting can be effectively removed.

In Sec. V, we described LMR experiments as a competition between the intrinsic quantum effect arising from the chiral anomaly and the classical effects of current jetting. The former describes a phenomenon intrinsic to massless chiral fermions. To see it in full force, the applied B should exceed B_Q, the field needed to move ζ into the LLL. This point seems worth emphasizing because in many reports the claimed anomaly seems to appear in weak fields, $B \ll B_Q$. The experimental concern is that once current jetting appears (at the field scale B_{cyc}), it inevitably engenders a dominant, negative LMR profile that is extrinsic in origin. The divergent field profiles of R_{spine} and R_{edge} provide a strong warning that the LMR profile is then highly unlikely to be intrinsic.

Looking ahead, we discussed in Sec. V how the classical screening effect from current jetting may be avoided by using ultrathin, gateable films of the Weyl semimetals, which may become available in the near future. For the fourth class of chiral anomaly semimetal $ZrTe_5$ [23,24], we propose using a focused ion beam to sculpt platelike samples that are 10 μm on a side, and applying microlithography to attach contacts for the squeeze test.

ACKNOWLEDGMENTS

The research was supported by the U.S. Army Research Office (Grant No. W911NF-16-1-0116) and a MURI award for topological insulators (No. ARO W911NF-12-1-0461). N. P. O. acknowledges support from the Gordon and Betty Moore Foundation's Emergent Phenomena in Quantum Systems Initiative through Grant No. GBMF4539. The growth and characterization of crystals were performed by S. K. and R. J. C., with support from the National Science Foundation (NSF MRSEC Grant No. DMR 1420541). Work at UCLA was supported by the U.S. Department of Energy (DOE), Office of Basic Energy Sciences, Award No. DE-SC0011978.

[1] H. B. Nielsen and M. Ninomiya, *The Adler-Bell-Jackiw Anomaly and Weyl Fermions in a Crystal*, Phys. Lett. B **130**, 389 (1983).

[2] S. M. Young, S. Zaheer, J. C. Y. Teo, C. L. Kane, E. J. Mele, and A. M. Rappe, *Dirac Semimetal in Three Dimensions*, Phys. Rev. Lett. **108**, 140405 (2012).

[3] X. G. Wan, A. M. Turner, A. Vishwanath, and S. Y. Savrasov, *Topological Semimetal and Fermi-Arc Surface States in the Electronic Structure of Pyrochlore Iridates*, Phys. Rev. B **83**, 205101 (2011).

[4] C. Fang, M. J. Gilbert, X. Dai, and B. A. Bernevig, *Multi-Weyl Topological Semimetals Stabilized by Point Group Symmetry*, Phys. Rev. Lett. **108**, 266802 (2012).

[5] B.-J. Yang and N. Nagaosa, *Classification of Stable Three-Dimensional Dirac Semimetals with Nontrivial Topology*, Nat. Commun. **5**, 4898 (2014).

[6] Z. J. Wang, Y. Sun, X. Q. Chen, C. Franchini, G. Xu, H. M. Weng, X. Dai, and Z. Fang, *Dirac Semimetal and Topological Phase Transitions in A_3Bi ($A = Na, K, Rb$)*, Phys. Rev. B **85**, 195320 (2012).

[7] *Classical Theory of Gauge Fields*, edited by V. Rubakov (Princeton University Press, Princeton, NJ, 2002), Chaps. 15 and 17.

[8] S. L. Adler, *Axial-Vector Vertex in Spinor Electrodynamics*, Phys. Rev. **177**, 2426 (1969).

[9] J. S. Bell and R. Jackiw, *A PCAC Puzzle: $\pi^o \to \gamma\gamma$ in the σ-Model*, Nuovo Cimento **60A**, 47 (1969).

[10] *Introduction to Quantum Field Theory*, edited by M. E. Peskin and D. V. Schroeder (Westview Press, Boulder, Colorado, 1995), Chap. 19.

[11] *Anomalies in Quantum Field Theory*, edited by Reinhold A. Bertlmann (Clarendon Press, Oxford, 2011).

[12] K.-Y. Yang, Y.-M. Lu, and Y. Ran, *Quantum Hall Effects in a Weyl Semimetal: Possible Application in Pyrochlore Iridates*, Phys. Rev. B **84**, 075129 (2011).

[13] D. T. Son and B. Z. Spivak, *Chiral Anomaly and Classical Negative Magnetoresistance of Weyl Metals*, Phys. Rev. B **88**, 104412 (2013).

[14] S. A. Parameswaran, T. Grover, D. A. Abanin, D. A. Pesin, and A. Vishwanath, *Probing the Chiral Anomaly with Nonlocal Transport in Three-Dimensional Topological Semimetals*, Phys. Rev. X **4**, 031035 (2014).

[15] A. A. Burkov, *Negative Longitudinal Magnetoresistance in Dirac and Weyl Metals*, Phys. Rev. B **91**, 245157 (2015).

[16] J. Xiong, S. K. Kushwaha, T. Liang, J. W. Krizan, M. Hirschberger, W. Wang, R. J. Cava, and N. P. Ong, *Evidence for the Chiral Anomaly in the Dirac Semimetal* Na_3Bi, Science **350**, 413 (2015).

[17] M. Hirschberger, S. Kushwaha, Z. Wang, Q. Gibson, S. Liang, C. A. Belvin, B. A. Bernevig, R. J. Cava, and N. P. Ong, *The Chiral Anomaly and Thermopower of Weyl Fermions in the Half-Heusler GdPtBi*, Nat. Mater. **15**, 1161 (2016).

[18] X. Huang, L. Zhao, Y. Long, P. Wang, D. Chen, Z. Yang, H. Liang, M. Xue, H. Weng, Z. Fang, X. Dai, and G. Chen, *Observation of the Chiral-Anomaly-Induced Negative Magnetoresistance in 3D Weyl Semimetal TaAs*, Phys. Rev. X **5**, 031023 (2015).

[19] C.-L. Zhang *et al.*, *Signatures of the Adler-Bell-Jackiw Chiral Anomaly in a Weyl Fermion Semimetal*, Nat. Commun. **7**, 10735 (2016).

[20] R. D. dos Reis, M. O. Ajeesh, N. Kumar, F. Arnold, C. Shekhar, M. Naumann, M. Schmidt, M. Nicklas, and E. Hassinger, *On the Search for the Chiral Anomaly in Weyl Semimetals: The Negative Longitudinal Magnetoresistance*, New J. Phys. **18**, 085006 (2016).

[21] Y. Li, Z. Wang, P. Li, X. Yang, Z. Shen, F. Sheng, X. Li, Y. Lu, Y. Zheng, and Z.-A. Xu, *Negative Magnetoresistance in*

Weyl Semimetals NbAs and NbP: Intrinsic Chiral Anomaly and Extrinsic Effects, Front. Phys. **12**, 127205 (2017).

[22] J. Xiong, S. Kushwaha, J. Krizan, T. Liang, R. J. Cava, and N. P. Ong, *Anomalous Conductivity Tensor in the Dirac Semimetal* Na_3Bi, Europhys. Lett. **114**, 27002 (2016).

[23] Q. Li, D. E. Kharzeev, C. Zhang, Y. Huang, I. Pletikosić, A. V. Fedorov, R. D. Zhong, J. A. Schneeloch, G. D. Gu, and T. Valla, *Chiral Magnetic Effect in* $ZrTe_5$, Nat. Phys. **12**, 550 (2016).

[24] T. Liang *et al.*, *Anomalous Hall Effect in* $ZrTe_5$, Nat. Phys. **14**, 451 (2018)..

[25] A. A. Burkov, *Giant Planar Hall Effect in Topological Metals*, Phys. Rev. B **96**, 041110 (2017).